

pubs.acs.org/JPCC Article

Enhancing CO Oxidation Activity *via* Tuning a Charge Transfer Between Gold Nanoparticles and Supports

Haotian Yang,[#] Jiajie Cen,[#] Qiyuan Wu, Claron J. Ridge, Xiao Tong, Chenyu Zhou, Vijayen Veerasamy, Dong Su, C. Michael Lindsay, Mingzhao Liu,* and Alexander Orlov*



Cite This: J. Phys. Chem. C 2022, 126, 4836-4844



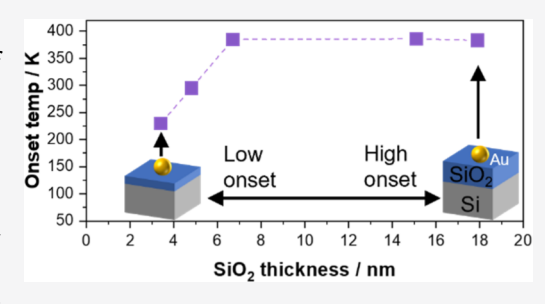
ACCESS I

Metrics & More

Article Recommendations

s Supporting Information

ABSTRACT: Charge transfer from the supports to nanoparticles at the interface is one of the key factors to determine the catalytic performances of supported nanoparticles. In this work, we showed in a systematic way that the charge transfer from semiconductor supports to Au nanoparticle catalysts can lower the onset temperature toward CO oxidation. For this study, a novel Au/SiO₂/Si composite system synthesized by the helium droplet deposition method with precisely tuned SiO₂ layer thickness was fabricated to control the magnitude of interfacial charge transfer. With the support of X-ray photoelectron spectroscopy and numerical simulations, it was demonstrated that the Schottky barrier formed across the Au/SiO₂/Si heterojunction led to a



negative charge accumulation on the surface of Au nanoparticles. In turn, this additional charge can be transferred to the antibonding orbital of adsorbed O₂ molecules to activate the O–O bonds, leading to enhanced CO oxidation. In addition to the charge transfer mechanism, the role of a strong electric field arising from the formation of the Schottky barrier was also explored to explain the observed enhancement of catalytic reactivity. Overall, this work highlights an important pathway for systematically tuning metal–support interactions to accelerate catalytic reactions and designing the next generation of nanocatalysts.

INTRODUCTION

Gold nanoparticles (Au NPs) supported on metal oxides have been widely studied for their high activity in a variety of important catalytic reactions. The literature shows that the catalytic performance is greatly affected by the type of supporting materials as the electronic metal—support interaction (EMSI) between metal NPs and supports is one of the key factors in determining the catalytic performances of supported metal NPs for important chemical reactions, including CO oxidation and water—gas shift (WGS) and hydrogenation reactions. The case of Au/TiO₂ catalysts, the EMSI could contribute to both improved sintering resistance of Au NPs and enhancement of interfacial charge transfer from the support to the Au NPs, which in turn contributes to an excellent catalytic performance of Au NPs.

Despite a general consensus on the importance of the EMSI, there is an ongoing debate on the exact charge state of catalytic Au NPs during the catalytic reaction, for example, whether they are positively or negatively charged. On one hand, the cationic gold species are regarded as active sites for CO oxidation. On the other hand, some recent publications pointed out that positively charged gold NPs lead to deactivation of the catalyst during the CO oxidation. In addition, several density functional theory (DFT) studies suggested that the activation energy toward CO oxidation is doubled by the positively charged gold clusters. It is also known that gold NPs can acquire partial negative charge from

lattice oxygen anions of the oxide support to activate CO oxidation at room temperature. This enhanced electron transfer could be beneficial to catalytic activity as described in several publications. $^{12-14}$ In the case of such semiconductor supports as ZnO and SiO₂/Si, the charge transfer leads to formation of a Schottky barrier at the metal—support interface. $^{15-17}$ However, the role of the electric field arising from the formation of the Schottky barrier is often overlooked for its role in catalytic enhancement. 18,19 The reason for this knowledge gap is that creating and studying model systems that allow fine tuning of the barrier and its associated electric field is a non-trivial task.

In this work, we have focused on overcoming this challenge by designing a model system that consists of uniform, finely dispersed gold NPs supported on a well-controlled oxide support. The Au NPs were synthesized in a special He nanodroplet deposition system located at the US Air Force Research Laboratory. More specifically, the Au NPs were deposited on oxide-covered Si wafers (SiO₂/Si), where the thickness of insulating layer was tuned by a controlled

Received: November 25, 2021 Revised: February 24, 2022 Published: March 8, 2022





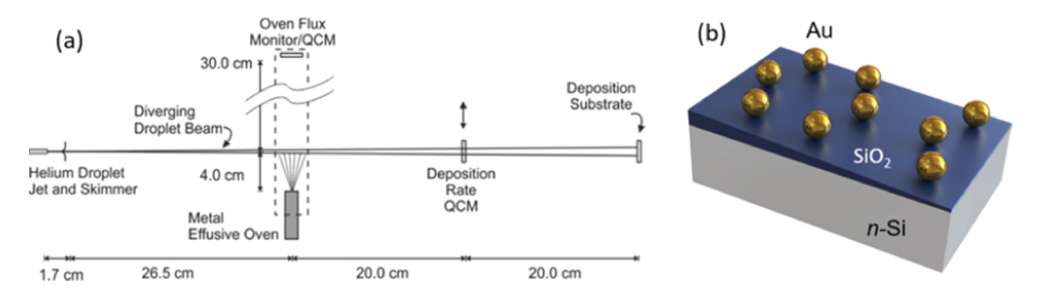


Figure 1. (a) Scheme of the He droplet deposition system. (b) Model of Au/SiO₂/Si heterojunctions. Adapted with permission from *The Journal of Physical Chemistry Letters* 2016, 7 (15), 2910-2914. Copyright 2016 American Chemical Society.

oxidation. This experimental design enabled a precise control of the interfacial charge transfer within the ${\rm Au/SiO_2/Si}$ heterojunction. By combining experiments and theoretical simulations, we discovered that the onset temperature for CO oxidation was reduced as the Au NPs became more negatively charged. Our results also highlight that a combination of both charge transfer and electric field formation at the metal–support interfaces is a major driving force for the superb reactivity of nano-sized Au NPs.

METHODS

Deposition of NPs by the He Nanodroplet Method.

Helium droplets were generated by supersonic expansion of He gas (99.9999%, chromatographic grade, Airgas Inc.) through a Pt nozzle (6.4 μ m in diameter) with a stagnation pressure of 100 bar into a vacuum chamber with a base pressure of 1×10^{-9} Torr (Figure 1a). The nozzle was cooled via a closed-cycle He compressor down to 6 K. A 0.05 cm skimmer, located at 1.7 cm in front of the nozzle, produced a diverging beam with a solid angle of 0.68 msr. After the skimmer, the beam was directed through a vacuum chamber with a base pressure of 1×10^{-9} Torr and equipped with up to three effusive ovens. At 6 K, helium droplets each containing \sim 5 × 10⁷ He atoms were produced and traveled above an effusive oven loaded with Au (99.99%). The Au atoms condensed into NPs within the He droplets and were carried to the substrates (SiO₂/Si wafers or TEM grids with SiO₂ windows), where the He droplets evaporated, leaving behind the Au NPs. Prior to the deposition of Au NPs, Si wafers [ntype with As dopant, (100) orientation] were cleaned in a hydrofluoric acid solution to remove the native oxide and then annealed in oxygen by rapid thermal processing (RTP-600S) at 1073 K for various duration of time to form SiO₂ layers of different thicknesses.

Transmission Electron Microscopy Characterizations. Transmission electron microscopy (TEM) images were acquired using a JEOL 2100 TEM system at 200 kV. In situ scanning transmission electron microscopy (STEM) imaging of Au NPs deposited on SiO_2 window TEM grids by the He droplet method was conducted using a Hitachi 2700 STEM system equipped with a Gatan in situ heating holder. The sample was first imaged at room temperature and then annealed at various temperatures with subsequent STEM imaging.

TPD and XPS Studies. Temperature-programmed desorption (TPD) and X-ray photoelectron spectroscopy (XPS) studies were conducted in a UHV chamber. For the TPD measurement, the sample was first heated to 473 K to remove residual gases absorbed on the surface before being cooled to 90 K with liquid N₂. Subsequently, with the sample held at 90

K, O_2 was dosed at 1×10^{-5} Torr for 15 min, followed by CO being dosed at 4×10^{-5} Torr for 15 min. The sample was then heated at a ramping rate of 30 K/min. During the TPD experiment, desorbed species were detected using a quadrupole mass spectrometer (MS). Measurements of catalytically produced CO₂ were based on the signal at m/z = 44. The XPS data were collected using a hemispherical electron energy analyzer (SPEC) with X-rays generated from an Al K α (1486.6 eV) source. Analysis of the XPS spectra was performed using CasaXPS software. The XPS binding energies were calibrated using the C 1s peak at 284.8 eV, with Shirley background being applied to all spectra. The validity of this calibration method across multiple samples was verified from the XPS spectra of Si 2p, which were contributed by both the Si wafer (Si⁰) and the SiO₂ layer (Si⁺⁴). As shown in Supporting Information, the Si⁰ 2p peak (99.4 eV) and the Si⁺⁴ 2p peak (103.5 eV) barely shifted across all samples, which validated our energy calibration.

Numerical Simulations of Barrier-Induced Charging of Au NPs. To evaluate the effect of the SiO_2 layer on the interfacial electric field and transfer, we conducted model-based numerical simulation using COMSOL Multiphysics software. Au/SiO₂/Si heterojunctions were modeled as capacitors, with a gold sphere (radius = 1.25 nm) and a flat silicon slab being considered as two electrodes. The two electrodes were separated by a flat slab of SiO_2 ($\varepsilon = 3.9$). Applied across the capacitor were biases of 0.48, 0.30, 0.25, 0.09, and 0 V, corresponding to the difference between binding energy (E_b) of negatively charged nanoparticulates and bulk Au derived from XPS results. By varying the thickness of the SiO_2 layer, the spatial distributions of electric field and charge densities were calculated.

■ RESULTS AND DISCUSSION

Previously, numerous studies have been conducted to control the size of metal NPs using various methods.²⁰⁻²⁵ However, there is a consensus that the majority of chemical synthetic procedures lead to surface contamination that can alter the catalytic activity of the NP-based catalysts. Alternatively, the size-selective method provides narrowly distributed and contamination-free NPs but suffers from a slow deposition rate. Therefore, employing a surfactant- and ligand-free approach with high NP yield is essential to fabricate a model system that allows a systematic exploration of the charge transfer mechanisms. The Au NPs utilized in this work were produced by the He nanodroplet method, where the lowtemperature He nanodroplets captured the metallic atoms that vaporized from the metal effusive oven and then carried the condensed metallic NPs inside to reach the target substrates. The He droplets evaporated after landing on substrates, leaving

ultra-clean metallic NPs on the substrates. The high deposition rate (10¹² nanoparticles/second)²⁶ is another advantage of this technique as compared to size-selected deposition. We previously demonstrated that size-controlled Au NPs deposited by the He nanodroplet method (Figure 1a) exhibited excellent stability,²⁷ making such a method a promising approach to fabricate the desired model system. This work was also the very first utilization of this method to fabricate catalytically active surfaces. Additional information about He nanodroplet deposition is presented in the Methods section. In this study, ultra-clean Au NPs with a very narrow size distribution were deposited on composite SiO₂/Si wafers, spanning a range of thicknesses of the SiO₂ layer. The resulting Au/SiO₂/Si heterojunctions (Figure 1b) were then utilized for either CO oxidation or characterization experiments.

Prior to helium nanodroplet deposition of Au NPs, Si wafers were cleaned in aqueous HF solution to remove the native oxide, followed by rapid thermal annealing in oxygen to generate SiO_2 layers of a well-defined thickness. Following the annealing period of time (t) ranging from 0 to 300, spectroscopic ellipsometry was employed to measure the thickness (d) of SiO_2 . The relationship between d and t is plotted in Figure S1 in the Supporting Information. As a result of different annealing times of the samples, the measured thicknesses of the SiO_2 layers were 3.4, 4.8, 6.7, 15.1, and 17.9 nm. Thereafter, the sample labeling followed the Au/Si-d format, where, for example, the sample containing a 3.4 nm-thick SiO_2 layer was labeled Au/Si-3.4.

To visualize the structure of Au/SiO₂/Si heterojunctions using TEM, the cross-sections of the samples were prepared using a focused ion beam (FIB) lift-out technique. Before the FIB lift-out, a ZnO layer was deposited on the surface of Au/SiO₂/Si samples by atomic layer deposition (ALD) technique to protect Au NPs from ion beam damage. The samples were used for TEM characterization only, while unprotected samples were used for CO oxidation experiments. The resulting cross-sectional images of sample Au/Si-3.4 clearly showed the presence of spherical and crystalline Au NP sitting on the surface of composite SiO₂/Si wafers (Figure 2). The

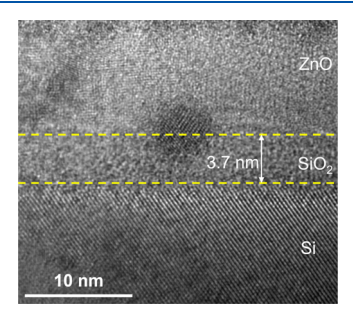


Figure 2. Structure of $Au/SiO_2/Si$ heterojunctions, sample Au/Si-3.4. SiO_2 layer were confirmed from the different contrast with the ZnO layer and Si substrate. Scale bar: 10 nm.

thickness of the SiO_2 interlayer was 3.7 nm, which was in good agreement with the ellipsometry results. The apparent embedding of the Au NP into the SiO_2 interlayer can be partially attributed to a sample view angle, where the cross-section was not perpendicular to the electron beam and thereby creating a perception of a partial sample encapsulation. Additional cross-sectional images of samples with different

 ${\rm SiO_2}$ thicknesses are shown in Figure S2 in the Supporting Information.

The direct characterization of ultra-small Au NPs in Au/Si-d samples using scanning electron microscope (SEM) was inaccurate as the small size of Au NPs was beyond the detection limit of SEM and only particles larger than 4 nm can could be measured. As a result, utilizing STEM was a better solution for determining the size distribution and thermal stability of Au NPs. To confirm reproducibility of Au particle sizes, the Au NPs were also deposited on SiO2 TEM grids using the He nanodroplet method to assess variation of particle sizes. Given that the same He nanodroplet deposition method was used to deposit Au NPs on both SiO2 TEM grids and Si/ SiO₂ substrates, the size and morphology of Au NPs is expected to be the same irrespective of the SiO₂ thickness. To confirm the stability of the samples under reaction conditions, in situ sample heating followed by STEM was conducted. Before heating, the Au NPs deposited on SiO₂ TEM grids had a narrow size distribution (Figure 3a), with the average diameter of Au NPs being 2.1 ± 0.5 nm. When the temperature was raised to 673 K, no significant agglomeration of Au NPs was observed with the average particle size remaining at 2.1 ± 0.6 nm (Figure 3b). These results demonstrate an excellent stability of our model system that is an important pre-requisite for conducting mechanistic catalytic studies.

To study the effect of SiO₂ layer thickness on catalytic performance, the samples containing variable thicknesses of Au/SiO₂/Si heterojunctions were tested for catalytic CO oxidation reaction using TPD. Catalytic conversion of CO to CO2 was followed using a mass spectrometer. The onset temperature for CO oxidation was used to illustrate the activation barrier differences between the samples in terms of CO oxidation.^{28,29} As summarized in Figure 4, the onset temperature was strongly correlated with the SiO2 layer thickness. For example, the onset temperature for sample Au/ Si-17.9 that has the thickest SiO₂ layer (17.9 nm) was 376 K. However, the temperature was reduced to 222 K for the sample with the thinnest SiO₂ layer (Au/Si-3.4). The decrease in onset temperature, however, was a non-uniform function of SiO₂ thickness. For example, a decrease in SiO₂ thickness from 17.9 to 6.7 nm resulted in a rather small onset temperature drop from 376 to 324 K. For SiO₂ layers thinner than 6.7 nm, the onset temperature decrease was much more dramatic, going down to 294 and 222 K for samples with 4.8 and 3.4 nm SiO₂ thickness, respectively. These decreases in onset temperatures can be explained by decreases in the activation barriers for CO oxidation. Different presentation of the TPD data can be found in Figure S3 in Supporting Information.

Additional characterization techniques included XPS, which showed variation in the chemical state of Au as a function of SiO_2 thickness (Figure 5). As the thickness of SiO_2 layers decreased, the Au $4f_{5/2}$ and Au $4f_{7/2}$ peaks shifted to lower binding energy (E_b). More specifically, the Au $4f_{5/2}$ peak shifted from 87.96 to 87.48 eV, while the Au $4f_{7/2}$ peak moved from 84.26 to 83.78 eV. It can be noted that the Au 4f peaks were less symmetric for samples with thinner SiO_2 layers (d < 7 nm). In addition to Au, we have also collected the Si 2p XPS spectra (Figure S4), which had contribution from both the Si wafer (Si^0) and the SiO_2 layer (Si^{+4}). Because the mean probe depth of XPS was approximately 10 nm, the Si^0 2p peak from the underlaying Si substrate attenuated with increasing SiO_2 thickness and eventually disappeared for the samples

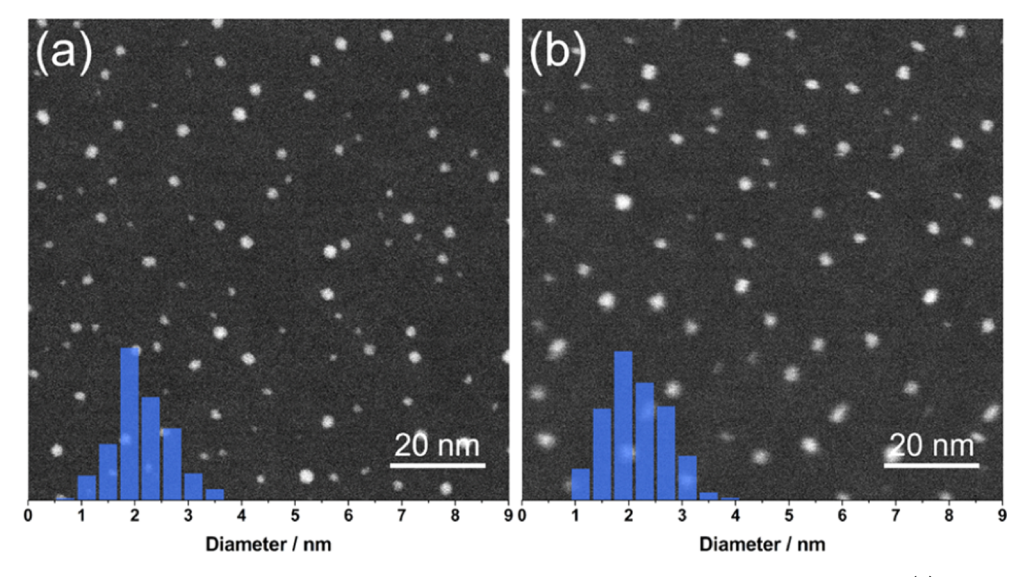


Figure 3. In situ STEM HAADF images of Au NPs supported on SiO₂ window along with NPs' size distributions at (a) room temperature and (b) 673 K. Scale bars: 20 nm.

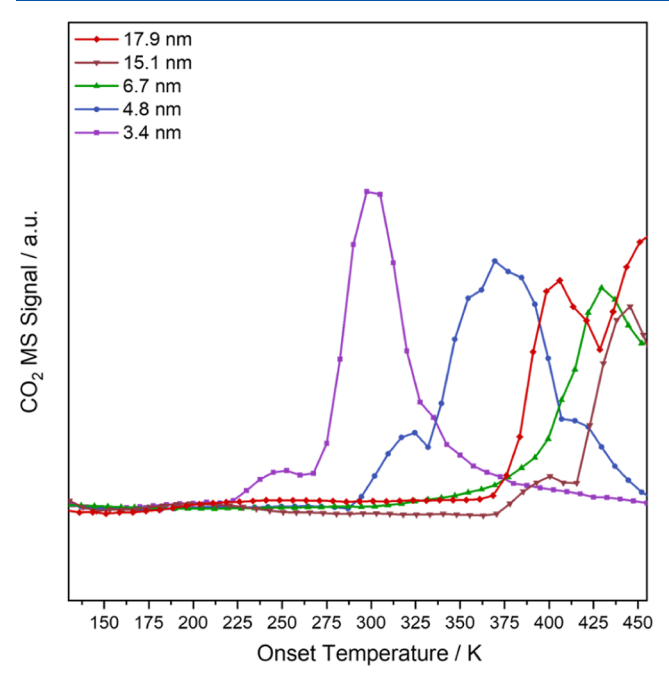


Figure 4. TPD results of Au/Si-d samples with different thicknesses of SiO₂.

containing SiO₂ layers thicker than 15 nm. For samples containing SiO₂ layers thinner than 7 nm, we observed a new peak at 89.6 eV that appeared next to the Au $4f_{5/2}$ peak (Figure 5). This peak, identified as a Si⁰ Auger line, disappeared for samples having SiO₂ layers thicker than 7 nm. Literature analysis indicated that in this energy range, there were two Si⁰ Auger lines, one was located at 89.6 eV and another positioned at 87.7 eV, where it overlapped with Au $4f_{5/2}$. These two peaks were also observed in the same E_b region for bare SiO₂/ Si wafers, with their intensity decreasing with an increase in thickness of SiO₂ layers. Therefore, a combination of these experimental observations confirms the Auger origin of the observed peaks (Supporting Information, Figure S5).

A further analysis to account for contribution from Si^0 Auger lines allowed us to isolate the Au $4\mathrm{f}_{5/2}$ and Au $4\mathrm{f}_{7/2}$ peaks,

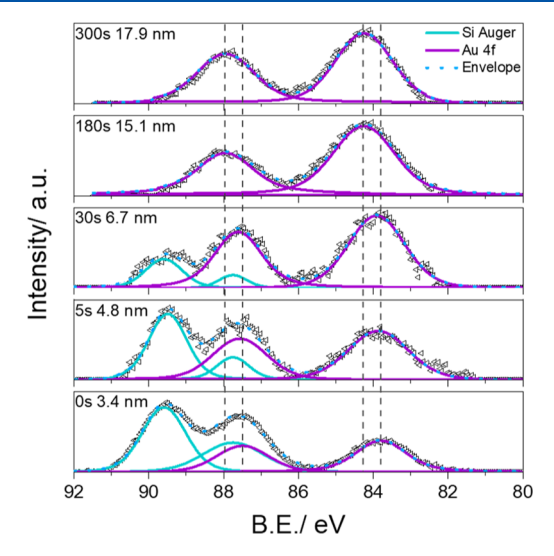


Figure 5. Au 4f XPS spectra of Au/Si-d samples with different thicknesses of ${\rm SiO_2}$.

thereby improving the quality of the fitting with a doublet. When the SiO_2 layer was thicker than 15 nm, the Au $4f_{5/2}$ and Au $4f_{7/2}$ peaks located at 87.96 and 84.26 eV were close to the E_b of the bulk Au.^{27,32} As the SiO₂ layer became thinner, both peaks shifted toward lower E_b. Figure 6b shows the dependence of E_b of the Au $4f_{7/2}$ shift on SiO_2 thickness, indicating a non-monotonous character of the $E_{\rm b}$ shift. This trend indicates a transfer of negative charges from n-Si substrates to Au NPs, which became more significant for a thinner SiO₂ layer. This charge transfer can be explained by a difference in Au NPs and n-Si work functions and the role of the Schottky barrier (Figure 6a). Given that Au has a larger work function (\sim 5.3 eV) than *n*-Si (\sim 4.2 eV), the *n*-type Schottky barrier was formed at the heterojunction, leading to a build-up of electric potential ΔV across the barrier. The electric potential can be calculated directly from the shift in Au $4f_{7/2}$ binding energy ΔV as a function of SiO₂ thickness (Figure 6b). An additional discussion of the Schottky barrier formation is presented in Supporting Information (Figure S6).

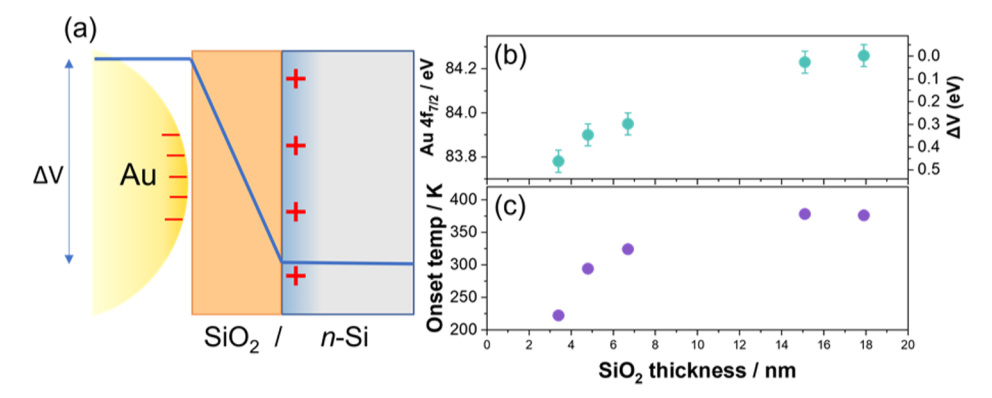


Figure 6. (a) Schematic representation of electric potential ΔV between Au and Si wafers for Au/Si-d samples. (b) Shift in Au $4f_{7/2}$ E_b and ΔV on the Au/Si-d samples. (c) Onset temperature of the CO oxidation reaction by TPD on the Au/Si-d samples.

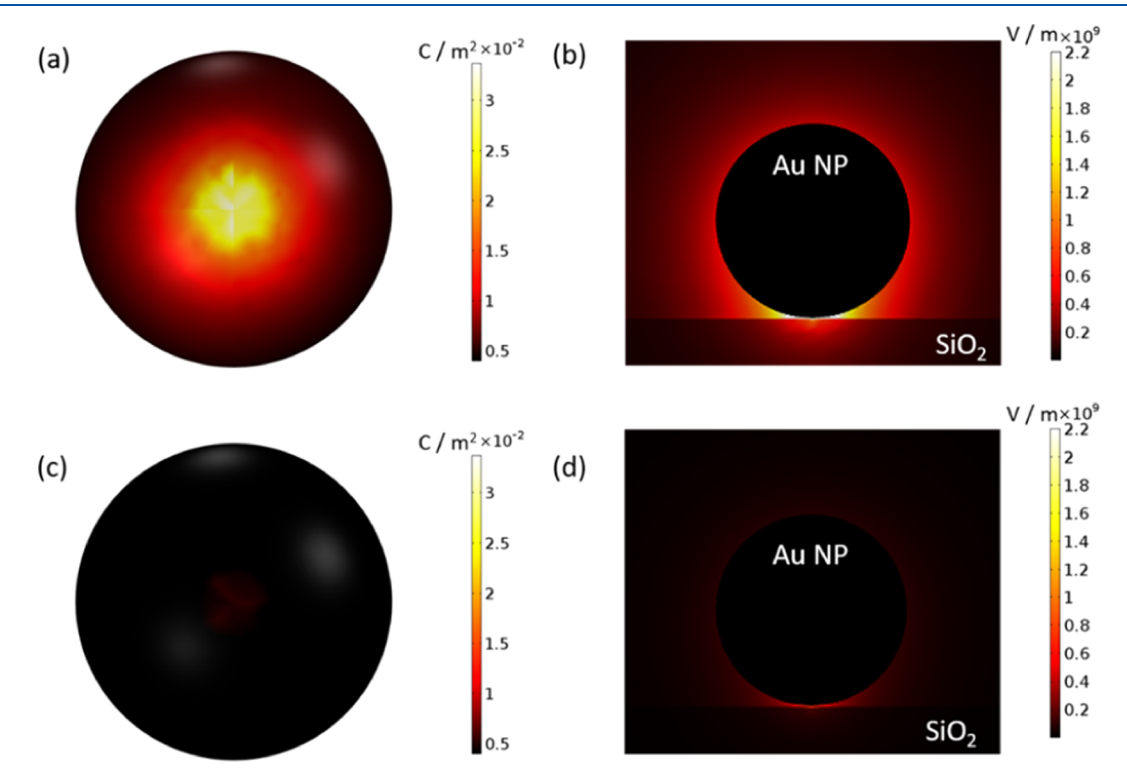


Figure 7. Simulation results of the Au/Si-3.4 (a,b) and Au/Si-15.1 samples (c,d). (a,c) Negative charge distribution at the bottom of the Au NPs; (b,d) cross-sectional electric field distribution near the Au/SiO_2 interface. The scale bars in figures indicate the change density and strength of the electric field given by the Au NP.

The electric charge on each Au NP can be calculated from the following expression

$$q = C_{\text{Au|Si}} \Delta V \tag{1}$$

in which C_{AulSi} is the capacitance of the Au NP/SiO₂/Si heterojunction. To quantitatively evaluate the capacitance and the charge distribution on Au NPs, we conducted numerical simulation of the Au/SiO₂/Si heterojunction using the finite element method (FEM). Briefly, the heterojunction was modeled as a capacitor, where a slab of SiO₂ was sandwiched between spherical Au particles and planar Si electrodes. Between the two electrodes, a bias ranging from 0 to 0.48 V was applied to replicate the experimentally determined ΔV . The numerical simulation based on Gauss's law gave the distributions of charge density and electric field. More specifically, we observed a charge accumulation at the bottom part of Au NPs, such as the part closest to the Si wafers.

Significantly, more negative charge accumulation was achieved in the sample with a thinner SiO₂ layer (Figure 7a). As a result, the electric field at the Au/SiO2 interface of Au/Si-3.4 was much stronger than that at the Au/Si-15.1 interface (Figure 7b,d). Simulation results across the range of SiO₂ thicknesses that included the capacitance (C_{AulSi}) , the charge on Au NPs (q), and the maximum electric field on the Au NP surface $(E_{\rm max})$ are summarized in Figure 8. As the thickness of SiO₂ decreased, C_{AulSi} increased slightly (Figure 8a). On the other hand, the electric charge (q) had a much stronger dependence on SiO₂ thickness than that for capacitance due to the ΔV term in eq 1 (Figure 8b). We calculated that the Au NPs in sample Au/Si-3.4 had a charge of $q = -1.16 \times 10^{-19}$ C, which meant that each Au NP carried 0.72 electrons on average. On the other hand, each Au NP present in sample Au/Si-15.1 would carry only 0.13 electrons on average, while sample Au/Si-17.9 would carry virtually none. It is important to note that the

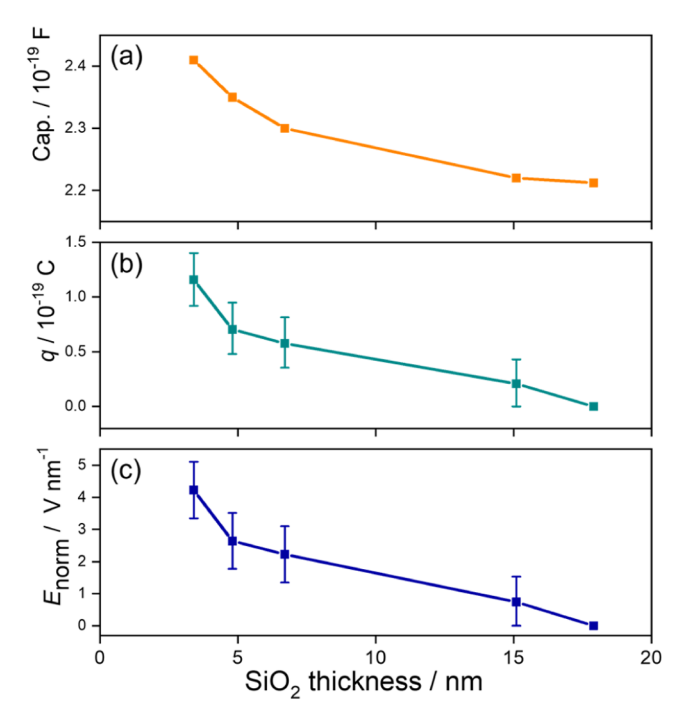


Figure 8. Summarized simulation results of the Au/Si-d samples. (a) Capacitance, (b) electric charge on each Au NP, and (c) strength of the electric field of the Au/Si-d samples. The strength of the electric field values is collected near the Au/SiO₂ interface, and these results indicate the maximum values of E_{norm} for the Au/Si-t samples.

error bars overlap for samples with ${\rm SiO_2}$ thickness larger than 15 nm, indicating that the charging effect becomes negligible for thicker samples. The maximum electric field on the Au NP surface ($E_{\rm max}$) followed a similar dependence on ${\rm SiO_2}$ thickness as that for ΔV , reaching about 4.2 V/nm in sample Au/Si-3.4 while dropping to 0.74 V/nm for Au/Si-15.19 (Figure 8c) and becoming negligible for sample Au/Si-17.9.

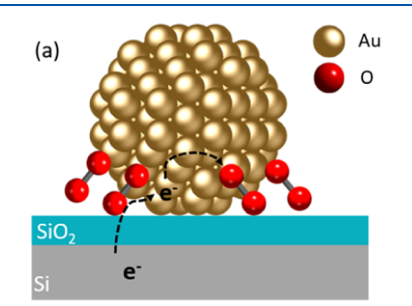
In order to understand the role of electron transfer and electric field in the Au/Si-d system, various mechanisms of CO oxidation were considered. In the case of Au NPs supported on reducible oxides, the Mars-van Krevelen-type mechanism suggests that CO is initially adsorbed at the perimeter of the Au-oxide interface and then reacts with oxygen in the oxide lattice, thereby leading to a partially reduced oxide support that is subsequently reoxidized with molecular oxygen. 33,34 However, in our system, the Au NPs were supported on non-reducible SiO $_2$ interlayers, and therefore, the Mars-van Krevelen mechanism cannot be invoked to explain the origin of the catalytic activity. Alternatively, we suggest that CO

oxidation follows the Langmuir–Hinshelwood mechanism, proposed by Widmann, Remediakis, and others. ^{33,35–37} In this mechanism, both reactants are adsorbed on the low-coordinated sites (steps and edges) ^{33,37} of Au NPs, where CO directly reacts with O_2 to form CO_2 .

Importantly, the dependence of CO oxidation onset temperature on SiO₂ interlayer thickness followed a very similar trend to that of ΔV , suggesting that negatively charged Au NPs were more catalytically active toward CO oxidation than the uncharged ones. However, it is important to highlight that both negative charge and strong electric field on the Au NP surface were the key factors for the observed dependence of catalytic reactivity on SiO₂ thickness. In terms of charge transfer, we estimate that the average of negative charge on each Au NP is about one electron. Therefore, this charge can be available for transfer to the antibonding orbital (π_g^*) of O_2 adsorbed on NPs of the Au/Si-3.4 sample, which can lead to weakening of the O-O bond and turning the O₂ molecule into a superoxide ion O_2^- (Figure 9). Previous studies by Hammer and co-workers demonstrated that a negative charge transferred from Au to anti-bonding orbitals of O2 stabilized the adsorbed O₂ and activated O₂ for CO oxidation.³⁸ On the other hand, the electron transfer was also beneficial for the CO chemisorption on Au NPs to facilitate the CO oxidation reaction. Kai and co-workers demonstrated that the negatively charged Au NPs supported on TiO2 adsorbed more CO as compared to Au NPs deposited on Al₂O₃ support, where the nonreducible Al₂O₃ was not donating electrons to Au NPs.³

In the case of electric field enhancement, we suggest that oxygen molecule polarization by the electric field can be a significant factor to explain our results. Although the charge transfer is often cited as the primary reason for improved catalytic activity of Au particles, 40-42 the role of electric field is an overlooked phenomenon for CO oxidation. In the case of CO₂ and methane, theoretical and experimental work by Zerbetto et al. 43,44 suggested a notable role of strong electric field for catalytic activity and selectivity enhancement. In our system, consisting of $Au/SiO_2/Si$ heterojunctions, the E_{max} remained below the threshold of a direct cleavage of the adsorbed O2. However, it was strong enough for the substantial rearrangement of the adsorbed O2 molecular orbitals, potentially leading to change in the electronic interactions between O_2 and Au NP surfaces, thus creating lower activation barriers for CO oxidation. Therefore, it is feasible to suggest that both electric field and charge transfer can significantly reduce the kinetic barrier for O-O bond cleavage and resulting CO oxidation.

It is worth noting that oxygen vacancies play a key role in Au NP-catalyzed CO oxidation. However, in our case, the SiO₂/Si



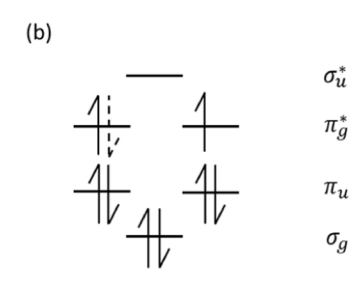


Figure 9. (a) Charge transfer effect on the polarization and activation of O_2 . (b) LUMO structure of O_2 absorbed on Au NPs with the charge transfer effect. The transferred electron is indicated by dashed arrow.

substrates were fully oxidized by rapid thermal treatment with O₂ at 800 °C. A complete oxidation of the SiO₂ interlayer was confirmed from the Si⁺⁴ peak originating from the oxidized surface and Si⁰ peaks originating from the underlying substrate, with no other oxidation states detected by the XPS results presented in Supporting Information. Given a low defect level in the fully oxidized and nonreducible nature of SiO₂, a variation in oxygen vacancy concentration and presence of active sites at the interface between Au NPs and supports are not expected to contribute to the observed variation in onset temperatures of our Au/Si-d system as compared to those with reducible supports. For example, in a classic Au/TiO $_2$ catalyst system, the activation of O2 can benefit from both increase in charge transfer and increased oxygen vacancies generated near the Au/TiO₂ interface. ^{49,50} In contrast, here we suggest that the thickness of SiO2 layers, rather than variation in oxygen vacancies and active sites at perimeter of Au NPs and SiO₂/Si, is the main factor that tunes both the charge transfer to Au NPs and the strength of electric field.

CONCLUSIONS

We designed a novel Au/SiO₂/Si heterojunction with controllable charge transfer to Au nanoparticles by varying the thickness of the SiO₂ interlayer. This model system allowed us to explore the charge transfer and electric field effects as the main factors affecting onset temperature of CO oxidation. More specifically, ultra-clean and uniform Au nanoparticles were deposited on low-defect SiO₂/Si wafers by the helium droplet deposition method. Complementary experiments that included in situ STEM, XPS, and TPD techniques, combined with theoretical simulations, were employed to systematically explore and tune negative charge transfer from n-type Si to Au NPs. Given the reproducible size distribution of Au NPs on low-defect and nonreducible SiO2 interlayers, the oxidation mechanism for the Au/Si-d system can be based on Au NPmediated reactions, where both reactants are adsorbed on the Au surface rather than at Au/SiO₂ interface. Therefore, various factors observed on reducible oxides that can influence the reaction rate, such as concentration of oxygen vacancies and interfacial active sites, can be considered as minor players in our system. Our results indicate that electron transfer and electric field were the primary origins of the enhanced reactivity. The electron transfer can promote the activation of O₂ to form superoxide O₂⁻ and CO adsorption. In addition, electric field can modify the electronic interactions between O₂ and Au NP surfaces, resulting in lower activation barriers for CO oxidation. It is likely that both electron transfer and electric field contributed to lowering the onset temperature of CO oxidation. As a result, the sample with the thinnest SiO₂ interlayer had the lowest onset temperature of 222 K, while the sample with the thickest SiO₂ interlayer had the highest onset temperature of 376 K. Future experiments, including atmospheric pressure reactor studies, will be conducted to understand the intrinsic reactivity of our system under dynamic reaction conditions. In addition, the planned experiments will explore charge transfer, electric fieldpromoted activation of O₂, mechanisms of CO adsorption, and interrelation between redox electronic properties in the Au/Si-d system. Our results provide a more sophisticated picture of the EMSI role in enhancing catalytic performance as compared to the published literature, thereby giving a more precise roadmap for a rational design of the next generation of nanocatalysts.

ASSOCIATED CONTENT

Supporting Information

The Supporting Information is available free of charge at https://pubs.acs.org/doi/10.1021/acs.jpcc.1c10072.

Plot of SiO_2 thickness vs oxidation time, Au nanoparticles on SiO_2 interlays with different thickness, CO oxidation TPD data, additional Si XPS data, and Schottky barrier formation (PDF)

AUTHOR INFORMATION

Corresponding Authors

Mingzhao Liu — Center for Functional Nanomaterials, Brookhaven National Laboratory, Upton, New York 11973, United States; orcid.org/0000-0002-0999-5214; Email: mzliu@bnl.gov

Alexander Orlov — Department of Materials Science and Chemical Engineering, Stony Brook University, Stony Brook, New York 11794, United States; Email: alexander.orlov@ stonybrook.edu

Authors

Haotian Yang — Department of Materials Science and Chemical Engineering, Stony Brook University, Stony Brook, New York 11794, United States; ⊚ orcid.org/0000-0003-3271-7420

Jiajie Cen – Department of Materials Science and Chemical Engineering, Stony Brook University, Stony Brook, New York 11794, United States

Qiyuan Wu — Department of Materials Science and Chemical Engineering, Stony Brook University, Stony Brook, New York 11794, United States; Present Address: Catalytic Carbon Transformation and Scale-up Center, National Renewable Energy Laboratory, Golden, CO, 80401, United States; orcid.org/0000-0002-8751-2003

Claron J. Ridge – Energetic Materials Branch, US Air Force Research Laboratory, Eglin Air Force Base, Florida 32542, United States

Xiao Tong — Center for Functional Nanomaterials, Brookhaven National Laboratory, Upton, New York 11973, United States

Chenyu Zhou — Department of Materials Science and Chemical Engineering, Stony Brook University, Stony Brook, New York 11794, United States; Center for Functional Nanomaterials, Brookhaven National Laboratory, Upton, New York 11973, United States; orcid.org/0000-0002-2749-4739

Vijayen Veerasamy — Department of Materials Science and Chemical Engineering, Stony Brook University, Stony Brook, New York 11794, United States

Dong Su — Center for Functional Nanomaterials, Brookhaven National Laboratory, Upton, New York 11973, United States; Present Address: Beijing National Laboratory for Condensed Matter Physics, Institute of Physics, Chinese Academy of Sciences, Beijing, 100190 China.;

orcid.org/0000-0002-1921-6683

C. Michael Lindsay – Energetic Materials Branch, US Air Force Research Laboratory, Eglin Air Force Base, Florida 32542, United States

Complete contact information is available at: https://pubs.acs.org/10.1021/acs.jpcc.1c10072

Author Contributions

*H.Y. and J.C. contributed equally.

Notes

The authors declare no competing financial interest.

ACKNOWLEDGMENTS

This research used resources of the Center for Functional Nanomaterials (CFN), which is a U.S. Department of Energy Office of Science User Facility, at the Brookhaven National Laboratory under contract no. DE-SC0012704. The authors also acknowledge NSF support from CBET award #2015275.

REFERENCES

- (1) Kung, M. C.; Davis, R. J.; Kung, H. H. Understanding Au-Catalyzed Low-Temperature CO Oxidation. *J. Phys. Chem. C* **2007**, 111, 11767–11775.
- (2) Bruix, A.; Rodriguez, J. A.; Ramírez, P. J.; Senanayake, S. D.; Evans, J.; Park, J. B.; Stacchiola, D.; Liu, P.; Hrbek, J.; Illas, F. A New Type of Strong Metal-Support Interaction and the Production of $\rm H_2$ through the Transformation of Water on $\rm Pt/CeO_2(111)$ and $\rm Pt/CeO_X/TiO_2(110)$ Catalysts. *J. Am. Chem. Soc.* **2012**, *134*, 8968–8974.
- (3) Campbell, C. T. Catalyst-Support Interactions: Electronic Perturbations. *Nat. Chem.* **2012**, *4*, 597–598.
- (4) Wang, Y.; Widmann, D.; Behm, R. J. Influence of TiO₂ Bulk Defects on CO Adsorption and CO Oxidation on Au/TiO₂: Electronic Metal—Support Interactions (EMSIs) in Supported Au Catalysts. ACS Catal. 2017, 7, 2339—2345.
- (5) Min, B. K.; Wallace, W. T.; Goodman, D. W. Synthesis of a Sinter-Resistant, Mixed-Oxide Support for Au Nanoclusters. *J. Phys. Chem. B* **2004**, *108*, 14609–14615.
- (6) Wang, Y.; Widmann, D.; Heenemann, M.; Diemant, T.; Biskupek, J.; Schlögl, R.; Behm, R. J. The Role of Electronic Metal-Support Interactions and Its Temperature Dependence: CO Adsorption and CO Oxidation on Au/TiO₂ Catalysts in The Presence of TiO₂ Bulk Defects. *J. Catal.* **2017**, 354, 46–60.
- (7) Zhou, X.; et al. Unraveling Charge State of Supported Au Single-Atoms During CO Oxidation. J. Am. Chem. Soc. 2018, 140, 554–557.
- (8) Wei, S.; Fu, X.-P.; Wang, W.-W.; Jin, Z.; Song, Q.-S.; Jia, C.-J. Au/TiO₂ Catalysts for CO Oxidation: Effect of Gold State to Reactivity. *J. Phys. Chem. C* **2018**, *122*, 4928–4936.
- (9) Tang, H.; et al. Ultrastable Hydroxyapatite/Titanium-Dioxide-Supported Gold Nanocatalyst with Strong Metal-Support Interaction for Carbon Monoxide Oxidation. *Angew. Chem., Int. Ed.* **2016**, 55, 10606–10611.
- (10) Wu, Z.; Zhou, S.; Zhu, H.; Dai, S.; Overbury, S. H. DRIFTS-QMS Study of Room Temperature CO Oxidation on Au/SiO₂ Catalyst: Nature and Role of Different Au Species. *J. Phys. Chem. C* **2009**, *113*, 3726–3734.
- (11) Green, I. X.; Tang, W.; McEntee, M.; Neurock, M.; Yates, J. T. Inhibition at Perimeter Sites of Au/TiO₂ Oxidation Catalyst by Reactant Oxygen. *J. Am. Chem. Soc.* **2012**, *134*, 12717–12723.
- (12) Xu, M.; He, S.; Chen, H.; Cui, G.; Zheng, L.; Wang, B.; Wei, M. TiO_{2-x}-Modified Ni Nanocatalyst with Tunable Metal–Support Interaction for Water–Gas Shift Reaction. *ACS Catal.* **2017**, *7*, 7600–7609.
- (13) Gunasooriya, G. T. K. K.; Seebauer, E. G.; Saeys, M. Ethylene Hydrogenation over Pt/TiO_2 : A Charge-Sensitive Reaction. *ACS Catal.* **2017**, *7*, 1966–1970.
- (14) Chua, Y. P. G.; Gunasooriya, G. T. K. K.; Saeys, M.; Seebauer, E. G. Controlling the CO Oxidation Rate over Pt/TiO₂ Catalysts by Defect Engineering of the TiO₂ Support. *J. Catal.* **2014**, *311*, 306–313
- (15) Bora, T.; Kyaw, H. H.; Sarkar, S.; Pal, S. K.; Dutta, J. Highly Efficient ZnO/Au Schottky Barrier Dye-Sensitized Solar Cells: Role of Gold Nanoparticles on The Charge-Transfer Process. *Beilstein J. Nanotechnol.* **2011**, *2*, 681–690.

- (16) Wager, J. F. Transparent Electronics: Schottky Barrier and Heterojunction Considerations. *Thin Solid Films* **2008**, *516*, 1755–1764
- (17) Kimoto, K.; Tada, T.; Kanayama, T. Modulation of CoSi₂/Si Schottky Barrier Height by Charge Transfer Doping Utilizing Cesium Segregation at the SiO₂/Si Interface. *Jpn. J. Appl. Phys.* **2007**, *46*, L110–L112.
- (18) Porosoff, M. D.; Yan, B.; Chen, J. G. Catalytic Reduction of CO₂ by H₂ for Synthesis of CO, Methanol and Hydrocarbons: Challenges and Opportunities. *Energy Environ. Sci.* **2016**, *9*, 62–73.
- (19) Yan, B.; Yao, S.; Kattel, S.; Wu, Q.; Xie, Z.; Gomez, E.; Liu, P.; Su, D.; Chen, J. G. Active Sites for Tandem Reactions of CO₂ Reduction and Ethane Dehydrogenation. *Proc. Natl. Acad. Sci. U. S. A.* **2018**, *115*, 8278–8283.
- (20) Wu, Q.; Xiong, S.; Shen, P.; Zhao, S.; Li, Y.; Su, D.; Orlov, A. Exceptional Activity of Sub-Nm Pt Clusters on CdS for Photocatalytic Hydrogen Production: A Combined Experimental and First-Principles Study. *Catal. Sci. Technol.* **2015**, *5*, 2059–2064.
- (21) Cargnello, M.; Doan-Nguyen, V. V. T.; Gordon, T. R.; Diaz, R. E.; Stach, E. A.; Gorte, R. J.; Fornasiero, P.; Murray, C. B. Control of Metal Nanocrystal Size Reveals Metal-Support Interface Role for Ceria Catalysts. *Science* **2013**, *341*, 771–773.
- (22) Mostafa, S.; Behafarid, F.; Croy, J. R.; Ono, L. K.; Li, L.; Yang, J. C.; Frenkel, A. I.; Cuenya, B. R. Shape-Dependent Catalytic Properties of Pt Nanoparticles. *J. Am. Chem. Soc.* **2010**, *132*, 15714–15719.
- (23) Schweinberger, F. F.; Berr, M. J.; Döblinger, M.; Wolff, C.; Sanwald, K. E.; Crampton, A. S.; Ridge, C. J.; Jäckel, F.; Feldmann, J.; Tschurl, M.; et al. Cluster Size Effects in the Photocatalytic Hydrogen Evolution Reaction. *J. Am. Chem. Soc.* **2013**, *135*, 13262–13265.
- (24) Wu, Q.; Yan, B.; Cen, J.; Timoshenko, J.; Zakharov, D. N.; Chen, X.; Xin, H. L.; Yao, S.; Parise, J. B.; Frenkel, A. I.; et al. Growth of Nanoparticles with Desired Catalytic Functions by Controlled Doping-Segregation of Metal in Oxide. *Chem. Mater.* **2018**, *30*, 1585–1592.
- (25) Tong, X.; Benz, L.; Kemper, P.; Metiu, H.; Bowers, M. T.; Buratto, S. K. Intact Size-Selected Au_N Clusters on a $TiO_2(110)$ -(1 X 1) Surface at Room Temperature. *J. Am. Chem. Soc.* **2005**, 127, 13516–13518.
- (26) Emery, S. B.; Rider, K. B.; Little, B. K.; Lindsay, C. M. Helium Droplet Assembled Nanocluster Films: Cluster Formation and Deposition Rates. *J. Phys. Chem. C* **2013**, *117*, 2358–2368.
- (27) Wu, Q.; Ridge, C. J.; Zhao, S.; Zakharov, D.; Cen, J.; Tong, X.; Connors, E.; Su, D.; Stach, E. A.; Lindsay, C. M.; et al. Development of a New Generation of Stable, Tunable, and Catalytically Active Nanoparticles Produced by the Helium Nanodroplet Deposition Method. *J. Phys. Chem. Lett.* **2016**, *7*, 2910–2914.
- (28) Peterson, E. J.; DeLaRiva, A. T.; Lin, S.; Johnson, R. S.; Guo, H.; Miller, J. T.; Hun Kwak, J.; Peden, C. H. F.; Kiefer, B.; Allard, L. F.; et al. Low-Temperature Carbon Monoxide Oxidation Catalysed by Regenerable Atomically Dispersed Palladium on Alumina. *Nat. Commun.* **2014**, *5*, 4885.
- (29) Ressler, T.; Walter, A.; Huang, Z.; Bensch, W. Structure and Properties of a Supported MoO₃–SBA-15 Catalyst for Selective Oxidation of Propene. *J. Catal.* **2008**, *254*, 170–179.
- (30) Whaley, R.; Thomas, E. W. Auger Spectra Induced by Ne⁺ and Ar⁺ Impact on Mg, Al, and Si. *J. Appl. Phys.* **1984**, *56*, 1505–1513.
- (31) Maydell, E. A. Caesium-Ion-Induced Auger Emission from Aluminium and Silicon. Surf. Interface Anal. 1992, 19, 65–70.
- (32) Wu, Q.; Cen, J.; Zhao, Y.; Tong, X.; Li, Y.; Frenkel, A. I.; Zhao, S.; Orlov, A. A Comprehensive Study of Catalytic, Morphological and Electronic Properties of Ligand-Protected Gold Nanoclusters Using XPS, STM, XAFS, and TPD Techniques. *Phys. Chem. Chem. Phys.* **2018**, *20*, 1497–1503.
- (33) Widmann, D.; Behm, R. J. Activation of Molecular Oxygen and the Nature of the Active Oxygen Species for CO Oxidation on Oxide Supported Au Catalysts. *Acc. Chem. Res.* **2014**, *47*, 740–749.
- (34) Ishida, T.; Murayama, T.; Taketoshi, A.; Haruta, M. Importance of Size and Contact Structure of Gold Nanoparticles

for the Genesis of Unique Catalytic Processes. Chem. Rev. 2020, 120, 464 - 525

- (35) Remediakis, I. N.; Lopez, N.; Nørskov, J. K. CO Oxidation on Rutile-Supported Au Nanoparticles. Angew. Chem., Int. Ed. Engl. 2005, 44, 1824-1826.
- (36) Widmann, D.; Liu, Y.; Schüth, F.; Behm, R. J. Support Effects in the Au-Catalyzed CO Oxidation—Correlation between Activity, Oxygen Storage Capacity, and Support Reducibility. J. Catal. 2010,
- (37) Schubert, M. M.; Hackenberg, S.; van Veen, A. C.; Muhler, M.; Plzak, V.; Behm, R. J. CO Oxidation over Supported Gold Catalysts— "Inert" and "Active" Support Materials and Their Role for the Oxygen Supply During Reaction. J. Catal. 2001, 197, 113-122.
- (38) Molina, L. M.; Hammer, B. Active Role of Oxide Support During CO Oxidation at Au/MgO. Phys. Rev. Lett. 2003, 90, 206102.
- (39) Yang, K.; Liu, J.; Si, R.; Chen, X.; Dai, W.; Fu, X. Comparative Study of Au/TiO2 and Au/Al2O3 for Oxidizing CO in the Presence of H₂ under Visible Light Irradiation. J. Catal. 2014, 317, 229-239.
- (40) Goodman, D. W. "Catalytically Active Au on Titania": Yet Another Example of a Strong Metal Support Interaction (SMSI)? Catal. Lett. 2005, 99, 1-4.
- (41) Sanchez, A.; Abbet, S.; Heiz, U.; Schneider, W.-D.; Häkkinen, H.; Barnett, R. N.; Landman, U. When Gold Is Not Noble: Nanoscale Gold Catalysts. J. Phys. Chem. A 1999, 103, 9573-9578.
- (42) Fu, Q.; Saltsburg, H.; Flytzani-Stephanopoulos, M. Active Nonmetallic Au and Pt Species on Ceria-Based Water-Gas Shift Catalysts. Science 2003, 301, 935-938.
- (43) Calvaresi, M.; Martinez, R. V.; Losilla, N. S.; Martinez, J.; Garcia, R.; Zerbetto, F. Splitting CO₂ with Electric Fields: A Computational Investigation. J. Phys. Chem. Lett. 2010, 1, 3256-3260.
- (44) Che, F.; Gray, J. T.; Ha, S.; Kruse, N.; Scott, S. L.; McEwen, J.-S. Elucidating the Roles of Electric Fields in Catalysis: A Perspective. ACS Catal. 2018, 8, 5153-5174.
- (45) Che, F.; Gray, J. T.; Ha, S.; McEwen, J.-S. Catalytic Water Dehydrogenation and Formation on Nickel: Dual Path Mechanism in High Electric Fields. J. Catal. 2015, 332, 187-200.
- (46) Kotobuki, M.; Leppelt, R.; Hansgen, D. A.; Widmann, D.; Behm, R. J. Reactive Oxygen on a Au/TiO2 Supported Catalyst. J. Catal. 2009, 264, 67-76.
- (47) Maeda, Y.; Iizuka, Y.; Kohyama, M. Generation of Oxygen Vacancies at a Au/TiO2 Perimeter Interface During CO Oxidation Detected by in situ Electrical Conductance Measurement. J. Am. Chem. Soc. 2013, 135, 906-909.
- (48) Zheng, X.; Veith, G. M.; Redekop, E.; Lo, C. S.; Yablonsky, G. S.; Gleaves, J. T. Oxygen and CO Adsorption on Au/SiO₂ catalysts Prepared by Magnetron Sputtering: The Role of Oxygen Storage. Ind. Eng. Chem. Res. 2010, 49, 10428-10437.
- (49) Yoon, B.; Häkkinen, H.; Landman, U.; Wörz, A. S.; Antonietti, J.-M.; Abbet, S.; Judai, K.; Heiz, U. Charging Effects on Bonding and Catalyzed Oxidation of CO on Au₈ Clusters on MgO. Science 2005, 307, 403-407,
- (50) Häkkinen, H.; Abbet, S.; Sanchez, A.; Heiz, U.; Landman, U. Structural, Electronic, and Impurity-Doping Effects in Nanoscale Chemistry: Supported Gold Nanoclusters. Angew. Chem., Int. Ed. Engl. 2003, 42, 1297-1300.

□ Recommended by ACS

In situ Dispersed Nano-Au on Zr-Suboxides as Active Cathode for Direct CO₂ Electroreduction in Solid Oxide **Electrolysis Cells**

Lixiao Zhang, Weishen Yang, et al.

AUGUST 06, 2021 NANO LETTERS

RFAD

Supported AuCu Alloy Nanoparticles for the Preferential Oxidation of CO (CO-PROX)

Tanna Elyn Rodrigues Fiuza and Daniela Zanchet

DECEMBER 30, 2019

ACS APPLIED NANO MATERIALS

READ Z

Compensation Effect Exhibited by Gold Bimetallic Nanoparticles during CO Oxidation

Joe Brindle and Michael M. Nigra

SEPTEMBER 09, 2021

ACS OMEGA

READ [7

Bridge Sites of Au Surfaces Are Active for Electrocatalytic CO₂ Reduction

Zixu Tao, Hailiang Wang, et al.

MAY 04, 2022

JOURNAL OF THE AMERICAN CHEMICAL SOCIETY

READ Z

Get More Suggestions >